Fission Gas Diffusion and Release for Cr 2 O 3 - Doped UO 2: From the Atomic to the Engineering Scale

Fission gas diffusion and release for Cr2O3-doped UO2: From the atomic to the engineering scale

Cooper, Michael William Donald
Pastore, Giovanni
Che, Yifeng
Matthews, Christopher
Forslund, Axel
Stanek, Christopher Richard
Shirvan, Koroush
Gamble, Kyle A.
Mays, Brian
Andersson, Anders David Ragnar

To be published in: Journal of Nuclear Materials

DOI to publisher's version: 10.1016/j.jnucmat.2020.152590

Journal Pre-proof

Fission Gas Diffusion and Release for Cr_2O_3-Doped UO_2: From the Atomic to the Engineering Scale

M.W.D. Cooper, G. Pastore, Y. Che, C. Matthews, A. Forslund, C.R. Stanek, K. Shirvan, T. Tverberg, K.A. Gamble, B. Mays, D.A. Andersson

PII: S0022-3115(20)31198-3
DOI: https://doi.org/10.1016/j.jnucmat.2020.152590
Reference: NUMA 152590

To appear in: *Journal of Nuclear Materials*

Received date: 15 June 2020
Revised date: 8 October 2020
Accepted date: 9 October 2020

Please cite this article as: M.W.D. Cooper, G. Pastore, Y. Che, C. Matthews, A. Forslund, C.R. Stanek, K. Shirvan, T. Tverberg, K.A. Gamble, B. Mays, D.A. Andersson, Fission Gas Diffusion and Release for Cr_2O_3-Doped UO_2: From the Atomic to the Engineering Scale, *Journal of Nuclear Materials* (2020), doi: https://doi.org/10.1016/j.jnucmat.2020.152590

Fission Gas Diffusion and Release for Cr_2O_3-Doped UO_2: From the Atomic to the Engineering Scale

M. W. D. Cooper[a], G. Pastore[b], Y. Che[c], C. Matthews[a], A. Forslund[d], C. R. Stanek[a], K. Shirvan[c], T. Tverberg[e], K. A. Gamble[b], B. Mays[f], D. A. Andersson[a]

[a]*Materials Science and Technology Division, Los Alamos National Laboratory P.O. Box 1663, Los Alamos, NM 87545, USA*
[b]*Computational Mechanics and Materials Department, Idaho National Laboratory, Idaho Falls, ID 83415, USA*
[c]*Department of Nuclear Science and Engineering, Massachusetts Institute of Technology, Cambridge, MA 02139, USA*
[d]*Kungliga Tekniska Högskolan (KTH), Stockholm, Sweden*
[e]*OECD Halden Reactor Project, Institute for Energy Technology, Os alle 5, 1777 Halden, Norway*
[f]*Framatome Inc., 3315 Old Forest Road, Lynchburg, VA 24501, USA*

Abstract

The anticipated benefits of large grains in Cr_2O_3-doped UO_2 pellets include improved mechanical and fission gas retention properties. To support the assessment of fission gas release (FGR) from doped pellets, the impact of doping on fission gas diffusivity for in-reactor conditions must be understood. In this work, we tackle this issue by informing the fission gas model within the BISON fuel performance code using material models developed at the atomic scale. The investigation of intra-granular fission gas diffusivity in Cr_2O_3-doped UO_2 is carried out by adapting a cluster dynamics model that, accounting for UO_2 thermochemistry, is capable of describing Xe diffusion under irradiation in undoped UO_2 as the starting point. Using a thermodynamic analysis, it is shown that in stoichiometric UO_2 with additions of Cr_2O_3, the oxygen potential is defined by the Cr-Cr_2O_3 two-phase equilibrium. Using the cluster dynamics model, the predicted Xe diffusivity in doped UO_2 was significantly increased in both the intrinsic and irradiation-enhanced regimes compared to undoped UO_2, as a result of higher concentrations of uranium and oxygen vacancies, respectively. This is a consequence of the more oxidizing conditions at high temperature, and more reducing conditions at low temperature, as a result of doping. Arrhenius functions have been fitted to the cluster dynamics results to enable implementation of the new diffusivities in the BISON fission gas behavior model. BISON simulations were carried out, showing the competing effects of the enlarged grains and the new fission gas diffusivity model, which act to suppress and enhance fission gas release, respectively. The new physics-informed model was validated against in-reactor experimental measurements under normal operation. Additionally, benchmarking was carried out for power ramp conditions. The predicted fission gas release agreed well with the experimental data, showing noticeable improvements over the standard UO_2 model.

1. Introduction

UO_2 has been the dominant nuclear fuel material for commercial light water reactors (LWRs) since their conception. Many of the standard UO_2 material properties make it suitable for LWR operation, including the accommodation of non-stoichiometry and fission products, a high melting point, radiation tolerance, and chemical stability [1]. The extensive operational experience in LWRs makes UO_2 a well understood and predictable fuel. Advanced fuel concepts are under development for use in LWRs in order to potentially provide enhanced fuel

performance and/or better economics than conventional UO_2. Typically, compounds with high thermal conductivity and high U density are considered, such as U_3Si_2 [2], as those are the main deficiencies of UO_2. Alternatively, more incremental advanced-UO_2 concepts have been developed that can inherit much of the operational experience and property characterization accumulated for standard UO_2 fuel. A range of additives, such as the oxides of Cr, Nb, Mg, and Ti, have been combined with UO_2 during fabrication to alter the microstructure of the fuel pellet [3–9]. In particular, fuel vendors have developed advanced oxide fuel concepts by doping UO_2 with Cr_2O_3 (Cr-doped) or with a mixture of Cr_2O_3 and Al_2O_3 (Cr+Al-doped) to enhance grain growth during fabrication [3]. While the primary intended benefit of large grains is a reduction in the strength of the fuel to increase the pellet-cladding interaction (PCI) margins [10], they are also anticipated to enhance fission gas retention.

During fabrication, dopants are typically blended with UO_2 powder in quantities of around ~ 1000 wt. ppm, which is near the solubility limit at sintering temperatures [5, 11, 12]. Work by Bourgeois et al. showed that there is a peak of 70 μm in the grain size at the solubility limit [5]. Similarly, Arborelius et al. observed UO_2 grain sizes of 44 μm for additions of 1000 wt. ppm Cr_2O_3, and 52 μm when co-doped with a mix of 500 wt. ppm Cr_2O_3 and 200 wt. ppm Al_2O_3 [3]. Bourgeois et al. showed further grain size enhancement could be attained through additions of dopant significantly in excess of the solubility limit, as long as temperatures exceed that of the CrO eutectic (1925 K) [5]. However, it is advantageous to limit dopant content to the solubility limit to minimize the potential impact on other material and neutronic fuel properties, while maintaining the benefits of large grains. From a fuel performance modeling perspective, this means a significant proportion of the UO_2 materials models, which have been well-validated with data from extensive experimental work and operational experience, could be inherited for doped UO_2. For example, the change in specific heat capacity, due to 1000 wt. ppm of doping, has been reported to be negligible by Arborelius et al. [3].

While it is unsurprising such small additions of dopant would not impact the specific heat capacity, other properties might be more sensitive to the composition of the fuel or the grain size. For example, the reduction in the fracture strength of standard UO_2 as a function of grain size was measured by Oguma [13]. Similarly, large grains cause smaller, but more numerous, cracks in the periphery of doped UO_2 pellets, which is beneficial in terms of PCI performace, compared to the fewer, larger cracks seen in undoped UO_2 [14]. Doped fuel has also shown improved creep, oxidation, and fuel washout behavior compared to conventional UO_2 [15]. By increasing the intra-granular diffusion length, large grains also play a role in FGR that can be captured in the physics-based FGR and gaseous fuel swelling model developed by Pastore et al. [16–18] and implemented in BISON [19].

FGR is a multistep process: i) fission gas is produced by fission in the bulk UO_2 lattice, where unperturbed diffusion occurs; ii) trapping of the insoluble gas in intragranular bubbles and its resolution back into the lattice by irradiation occur and can be assumed to rapidly reach equilibrium under most conditions of practical interest [20, 21]; iii) the resultant concentration of gas in the bulk diffuses to the grain boundaries (with the diffusion rate during equilibrium trapping and resolution captured by an effective diffusion coefficient) and forms inter-granular bubbles; and iv) growth of the inter-granular bubbles leads to fuel swelling, bubble interconnection, and gas release upon the formation of pathways to a free surface [17]. The fission gas behavior model in BISON incorporates the above processes in order to calculate the coupled fission gas release and swelling concurrently [16–18]. Owing to its physical basis, the model, which was originally developed for standard UO_2 fuel, can be leveraged for the analysis of other fuel types, such as Cr-doped UO_2, provided that the values for the physical parameters are adapted. For instance, the grain size is a key model parameter that reduces the rate of gas arriving at inter-granular bubbles (lowering FGR) by increasing the intra-granular diffu-

sion length. The gas atom diffusivity in the bulk is another key parameter that affects the gas diffusion rate to grain boundaries.

Che et al. demonstrated the use of this FGR model for fuel performance modeling of large-grain doped UO_2 [22]. In that work, an empirically tuned enhanced effective diffusivity, based on experimental observation by Killeen [4], across all temperatures as a preliminary approach to account for the diffusivity enhancement in Cr-doped UO_2 compared to undoped UO_2, showing good agreement with Halden FGR validation tests. Here, we build upon the work of Che et al. [22] by investigating the origins of the enhanced effective diffusivity through the impact of the dopant on the unperturbed fission gas diffusivity. The objective is to produce a mechanistically-derived doped UO_2 diffusivity model capturing the temperature dependence in enhancement (or suppression), as expected in an activated process governed by Arrhenius laws.

Experimental results on fission gas diffusivity in doped and undoped UO_2 are shown in Figure 1. Data from Killeen [4] and Kashibe and Une [24] indicate that Cr-doped UO_2 can exhibit higher fission gas diffusivity than undoped UO_2. Killeen only provides a single doped and a single undoped UO_2 data point, making it impossible to determine the temperature dependence of the respective diffusivities. On the other hand, Kashibe and Une [24] measured fission gas diffusivity for doped and undoped UO_2 between 1472 K and 1878 K. Above 1525 K, the diffusivity is greater in doped UO_2 than undoped UO_2 by up to a factor of 1.9, whereas below 1525 K it is suppressed. The activation energy for fission gas is 0.54 eV greater in doped UO_2 compared to undoped UO_2.

Three temperature regimes exist for unperturbed fission gas diffusion in UO_2 during reactor operation [23]: D_1 intrinsic diffusion at high temperatures ($T \gtrsim$1650 K), which is equivalent to out-of-pile diffusion, D_2 irradiation-enhanced diffusion at intermediate temperatures (1650 K $\gtrsim T \gtrsim$ 1300 K), and D_3 athermal irradiation driven diffusion at low temperatures (1300 K $\gtrsim T$). The in-reactor Killeen data points [4] were taken at high temperatures where D_1 is dominant. The samples used for the Kashibe and Une data [24] were irradiated to introduce fission gas but were assessed for out-of-pile conditions and they only indicate the effect of doping on D_1. By comparison, the undoped UO_2 data used by Turnbull et al.were taken under irradiation and over a wide range of temperatures representing D_2 and D_3 [23], which were combined with the Davis and Long data on D_1 [25] to give a description of fission gas diffusivity over the full temperature range. The objective of this work is to provide a similar understanding of D_1, D_2, and D_3 for doped UO_2. It is clear from Figure 1 that there is significant variability for D_1 diffusivity, be it for out-of-pile or high temperature in-pile fuel samples. This is likely caused by different oxygen potentials and deviations from stoichiometry in $UO_{2\pm x}$, which strongly influences the concentration of the defects responsible for diffusion.

Extensive atomic scale work has been undertaken to study fission gas behavior in undoped UO_2 [27–36]. Among other studies, our previous work [37], which was used as the foundation for the present study, employed density functional theory (DFT) calculations of enthalpy in conjunction with empirical potential entropy calculations to give accurate predictions of intrinsic Xe diffusion (D_1) by U vacancy assisted transport of Xe in U-O divacancies, $\{Xe : V_U : V_O\}$ (this modified Kröger-Vink notation indicates Xe accommodation within the vacancy cluster but without specifying a site). In the work of Perriot et al., a set of DFT data was generated that included large clusters of U and O vacancies containing Xe atoms [37]. A number of those large clusters exhibited low migration barriers however, under thermal equilibrium, their concentrations are not sufficient to contribute significantly to D_1 diffusion. In order to consider the role of defect production on diffusion (D_2), a cluster dynamics model formulated in terms of the free energy of the system (labeled free energy cluster dynamics or FECD) has been devloped [38, 39] using the DFT data from Perriot et al. [37].

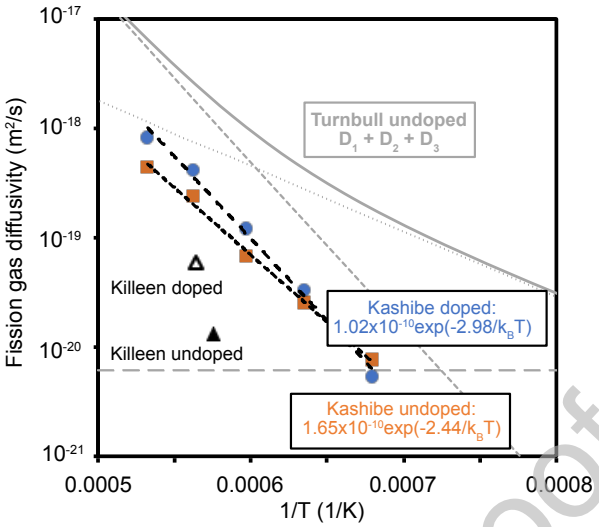

Figure 1: The out-of-pile diffusion data from Kashibe and Une [24] for Cr-doped (blue) and undoped UO_2 (orange). The increase in activation energy due to doping is 0.54 eV. The single Cr-doped (open triangle) and single undoped (closed triangle) UO_2 measurements from Killeen [4] are also shown. The description of fission gas diffusivity under irradiation for undoped UO_2 from Turnbull et al. [23, 26] is shown by the gray lines (dashed are separate contributions D_i, and the solid line is the total D) - D_1 is from the Davies and Long data [25]. Note that the Killeen (high temperature) data, and the Kashibe and Une (out-of-pile) data correspond to D_1, whereas the Turnbull model (in-pile, wide temperature range) includes contributions from D_1, D_2, and D_3.

Cluster dynamics simulations using the FECD model (as implemented in the Centipede code [39]) predict that under in-reactor conditions, the concentration of the large cluster $\{Xe : 4V_U : 3V_O\}$ is significantly enhanced by irradiation and is responsible for D_2 diffusion. Good agreement with the empirical Turnbull model for Xe diffusion in undoped UO_2 (as currently used in BISON) was obtained. In order to achieve this result, a very large number of clusters were considered, including Xe-bearing vacancy clusters consisting of 1-8 V_U associated with various numbers of V_O. Additionally, a critical consideration was the inclusion of the mobile $\{U_i : 2O_i\}$ clusters and their interaction with sinks, without which high concentrations of uranium interstitial species would suppress the concentration of $\{Xe : 4V_U : 3V_O\}$ through annihilation. In total, 48 defects and clusters were considered. Finally, it was important to consider the oxygen potential, which not only influences the stability of point defects in UO_2, but also, by extension, the number of oxygen vacancies in Xe-bearing clusters. This governs the mobility of such clusters and affects their contribution to the total Xe diffusivity.

Our hypothesis is that additions of Cr_2O_3 to UO_2 can change the oxygen potential and, therefore, the Xe diffusivity in doped UO_2 relative to undoped UO_2. More specifically, the possibility that the Cr-Cr_2O_3 two-phase equilibrium defines the oxygen potential in doped UO_2 for a wide range of reactor conditions is tested through thermodynamic investigation. The Cr-Cr_2O_3 two-phase oxygen potential is then implemented within the Centipede simulations of Xe diffusivity, showing that intra-granular diffusion is enhanced through doping. The new Xe diffusivities are implemented in BISON, and validated against experiments from the Halden

Reactor Project and transient tests carried out by the commercial fuel vendor Framatome.

2. Methods

2.1. Free energy cluster dynamics (FECD) model

The FECD framework was developed by Matthews et al. and is implemented in the Centipede code [38, 39]. The framework has been applied to the concentration and diffusivity of defects to describe self-diffusion [38] and Xe diffusion [39] in UO_2 under irradiation. The results demonstrate the successful application of this framework to capture the D_1-D_2 transition for self and Xe diffusion. In this work, we employ the Xe diffusion version [39] that was parameterized using DFT data published by Perriot et al. [37]. A detailed description of the framework can be found elsewhere [38, 39], while a brief description of the method will be given here for sake of completeness.

The concentrations of defects in the UO_2 system under irradiation are calculated by solving a set of ordinary differential equations (ODEs) that capture a number of phenomena including: production of Frenkel pairs through irradiation, mutual recombination of Frenkel pairs, interaction with sinks, and clustering of point defects. For the concentration, x_d, of a given defect, d, the ODE can be expressed as:

$$\frac{dx_d}{dt} = \dot{\beta}_d + \sum_C \dot{R}_{d,C}(x_d, x_C, T, G) - \sum_s \dot{S}_{d,s}(x_d, x_s, T, G) \tag{1}$$

where t is time, $\dot{\beta}_d$ describes the source rate of defects through irradiation, $\dot{R}_{d,C}$ and $\dot{S}_{d,s}$ are the cluster and sink rates, respectively, which depend on the defect concentration (x_d), the concentration of a given cluster (x_C), the sink concentration (x_s), the temperature T, and the Gibbs free energy of the system G. Centipede simulations find the steady-state solution to this coupled set of ODEs, such that $\frac{dx_d}{dt} \leq \mathcal{R}$ for all defects, where $\mathcal{R}$ is the convergence criteria. The reaction rate, $\dot{R}_d$, for a given reaction, $A + B \rightarrow Y + Z$, can be expressed as:

$$\dot{R}_d = \begin{cases} \frac{k_i^2}{\Omega} D x_A x_B \left[1 - exp\left(\frac{f}{k_B T}\right)\right], & \text{if } f < 0, \\ \frac{k_i^2}{\Omega} D x_Y x_Z \left[exp\left(\frac{f}{k_B T}\right) - 1\right], & \text{otherwise} \end{cases} \tag{2}$$

where k_B is the Boltzmann constant, Ω is the atomic volume, k_i is a reaction rate constant, and $D = D_A + D_B$ is the sum of the diffusivities of the reactants. x_A and x_B are the atom fractions of the reactants, and x_Y and x_Z are the atom fractions of the products. The driving force, f, is non-zero if a particular reaction is not at thermal equilibrium and it acts to return the system to equilibrium. If the driving force, f, is less than zero, the net rate is for the reaction to go forwards, otherwise it goes backwards. The driving force is given by the change in the free energy of the system due to the reaction:

$$f = \sum_{p \epsilon P} \frac{\partial G}{\partial x_p} - \sum_{r \epsilon R} \frac{\partial G}{\partial x_r} \tag{3}$$

where P and R are the set of products, p, and reactants, r, respectively. The free energy contributions from each defect (reactant or product) are given by the defect energies calculated by Perriot et al. [37]. A detailed explanation of the application of Eqs. (1) to (3) to Xe in UO_2 is given by Matthews et al. [38, 39].

2.2. BISON fuel performance simulations

Due to the relatively small concentration of chromia doped in UO_2 (~1000 wt. ppm), many standard undoped UO_2 properties are expected to be readily transferable to doped UO_2. Arborelius et al. measured the thermal diffusivity of fresh fuel, noting only a small change due to doping [3]. It is expected that this small difference will become negligible after some burnup, as the degradation in thermal conductivity will become dominated by the accumulation of fission products and irradiation induced defects. The larger grain size of doped UO_2 is expected to have a negligible effect on thermal transport, given that molecular dynamics (MD) simulations indicate grain size must be on the sub-micron scale to have a noticeable impact [40]. Therefore, the Halden thermal conductivity correlation for undoped UO_2, as a function of burnup (as documented in Refs. [19, 41]), is used for simulations of the Halden tests in this study. In the simulations of Framatome power ramp tests, the thermal conductivity model for undoped UO_2 from the Nuclear Fuels Industry Reseach (NFIR) Program is adopted [42]. It is noted that, due to the impact of doping on FGR (through the grain size and Xe diffusivity) and the degradation of thermal conductivity due to Xe in the lattice, there may be an indirect effect on thermal transport. Although the coupling of fission gas release to thermal conductivity has been omitted in this work, the doped UO_2 fission gas release models developed here could be used in conjuction with the multiscale thermal conductivity model of Tonks et al. [43] in future work.

The specific heat capacity of doped UO_2 has been noted to be within 3% of that for undoped UO_2 [3]. Therefore, we have applied the Fink data for undoped UO_2 [44] to doped UO_2. Arborelius et al. note that Cr+Al doped UO_2 has the same thermal expansion as undoped UO_2 [3]. Therefore, the standard BISON UO_2 thermal strain model [46] will be adopted here for Cr-doped UO_2. In BISON, the grain growth of standard UO_2 due to the high temperatures experienced in-reactor is described by the model from Ainscough et al. [47]. Although this model is also applied here for doped UO_2, it does not result in significant grain growth due to the large initial grain size of doped UO_2 (~ 40-70 μm). This behavior is expected due to the stability of large grains.

The fission gas behavior model for oxide fuel in BISON incorporates the fundamental physical mechanisms for FGR [17, 19]. The diffusion of fission gas from the bulk to the grain boundaries is governed by the unperturbed diffusivity of single gas atoms through the UO_2 lattice (D), trapping at intra-granular bubbles (g), and resolution from intra-granular bubbles (b). Transport from within a spherical grain (as assumed in this model [17]) to the grain boundary can be described by:

$$\frac{\partial C_{ig}}{\partial t} = \frac{b}{b+g} D \nabla^2 C_{ig} + \beta \tag{4}$$

where C_{ig} (atoms·m^{-3}) is the intra-granular gas concentration, g (s^{-1}) is the trapping rate, b (s^{-1}) is the resolution rate, D (m^{2}s^{-1}) is the unperturbed diffusivity, and β (atoms·s^{-1}) is the source term for the generation of gas atoms through fission. The effective diffusivity can be described as [20]:

$$D_{\text{eff}} = D \frac{b}{b+g} \tag{5}$$

The trapping and resolution parameters, g [48] and b [49], are given by:

$$g = 4\pi R N D \tag{6}$$

$$b = 3.03 \dot{F} \pi l_f (R + Z_0) \tag{7}$$

where $l_f = 6 \times 10^{-6}$ m is the length of a fission fragment track, $Z_0 = 10^{-9}$ m is the radius of influence of a fission fragment [49], and $\dot{F}$ is the fission rate density. The bubble radius and

bubble density, R and N respectively, are solved for during the BISON simulations using the model described by Pizzocri et al. [50].

The unperturbed fission gas diffusivity for undoped UO_2 is given by the Turnbull model [23, 26]:

$$D = D_1 + D_2 + D_3 \tag{8}$$

$$D_1 = 7.6 \times 10^{-10} \cdot \exp\left(-4.86 \times 10^{-19}/(k_B T)\right) \tag{9}$$

$$D_2 = 5.64 \times 10^{-25} \sqrt{\dot{F}} \cdot \exp\left(-1.91 \times 10^{-19}/(k_B T)\right) \tag{10}$$

$$D_3 = 8 \times 10^{-40} \dot{F} \tag{11}$$

where D_1, D_2, and D_3 represent the intrinsic, irradiation-enhanced, and athermal contributions to fission gas diffusivity, respectively. Since it is assumed that D_3 is unaffected by small additions of dopant, as it is driven by atomic mixing during high energy damage cascades, this work will focus on using atomistic simulations to predict the change in D_1 and D_2 due to Cr-doping. The fission gas model also accounts for the evolution of inter-granular bubbles, the associated gaseous fuel swelling, and the eventual saturation of the grain boundaries resulting in FGR to the fuel rod free volume. Swelling due to intra-granular bubbles is not considered in the present work, as it is generally less important than that due to inter-granular bubbles in UO_2 under normal operating conditions, at least for burnups below 45 GWd/t [45]. Further details of the fission gas model can be found in Refs. [16–19]. As Eq. (4) is solved, the effect of the grain size on the rate of diffusion to the grain boundaries is naturally accommodated for in the model. Note that there is also an effect of the grain size on the grain boundary stage of fission gas release (i.e. the grain surface-to-volume ratio affects the saturation behavior of grain boundaries and, consequently, the amount of gaseous swelling and FGR). In contrast to intra-granular diffusion, the surface-to-volume ratio effect on grain boundary bubble behavior tends to increase FGR with a larger grain size (see details given by Pastore at al. [18]).

While gaseous swelling is determined by the fission gas model and the effect of doping is accounted for by changes to the grain size and diffusivity within that model, swelling due to the accumulation of solid fission products is given by an empirical relation [46] and is assumed to be unchanged due to doping.

During irradiation nuclear fuel undergoes further densification beyond the beginning of life sintered density. Observations during the Halden Reactor Project [51, 52], showed that a densification of 0.1-0.2% occurred for Cr-doped UO_2 fuel rods. Therefore, the standard UO_2 densification ESCORE model [53] was used for doped UO_2 but with the maximum densification set to 0.15% in the simulations of the Halden tests. Densification information is not available for the Framatome ramps test, hence the standard value of 1% for undoped UO_2 is applied to doped UO_2. Such small additions of dopant are not expected to influence the uncracked elastic behavior and, as such, typical elastic constants for standard UO_2 are applied. Larger grains can reduce the fracture strength of UO_2 [13]. However, in the absence of a specific model for Cr-doped UO_2, the isotropic softening model for fuel cracking from Barani et al. for undoped UO_2 is used [54]. The creep rate is considered using the MATPRO correlations for standard UO_2 [46]. The creep model has not yet been developed for doped UO_2 and should be addressed in future work.

3. Results and Discussion

3.1. Thermodynamics of the Cr-U-O system

In this section, we discuss the influence that the Cr-Cr_2O_3 equilibrium has on the thermodynamics of the Cr-U-O system. Temperatures relevant to normal LWR operation are typically

below 1600 K for the centerline of the fuel pellet, which is the hottest part of the fuel (see Section 3.6). Extrapolation of a Cr_2O_3 solubility model [55] derived by analysis of experimental data under sintering conditions indicates that at reactor operating temperatures most of the dopant will be out-of-solution (asuming typical Cr_2O_3 additions of 1000 wt. ppm or more). Similarly, atomic scale calculations predict low solubility at temperatures relevant to steady-state reactor operation [56, 57]. For example, DFT calculations have been used to predict negligible solution of Cr below $\sim$ 1700 K [56]. Therefore, the incorporation of Cr as defects in the lattice is not expected for in-reactor conditions and cannot result in gas-dopant atomic scale binding that would interfere directly with the migration of fission gas. However, that does not mean that the presence of a Cr secondary phase does not impact the defect chemistry, and thus Xe diffusivity, of UO_2 indirectly. In this section, we investigate the possibility that additions of Cr_2O_3 to UO_2 can change the oxygen potential of the fuel pellet and influence the concentrations of vacancies that govern diffusion.

Figure 2 shows the oxygen potential of $UO_{2\pm x}$ as a function of temperature for fixed values of x. Here we define the oxygen potential as $k_B T \ln(P_{O_2})$, where the P_{O_2} is the oxygen partial pressure in atmospheres. Note that the chemical potential used within the Centipede code to determine defect stability also includes a reference O_2 energy. The results using the Calphad approach [58] implemented in Thermo-Calc [59], with a database combining the description of U-O from Guéneau et al. and the SGTE Substances database v6 (SSUB6) for Cr-O, are shown in Fig. 2A [60, 61], and Fig. 2B shows the results using the Lindemer and Besmann model [62]. The gray lines represent UO_{2+x}, the yellow lines represent UO_{2-x}, and the black lines represent exactly stoichiometric UO_2. The oxygen potential for the Cr-Cr_2O_3 two phase equilibrium is shown by the green line and is defined by the following reaction:

$$2/3 Cr_2O_3 \leftrightarrow 4/3 Cr + O_2 \tag{12}$$

In Figure 2A and B, the SSUB6 Calphad database [61] and JANAF data [63] were used, respectively. Comparison of A and B indicates similar behavior for both sets of data, particularly for the oxygen potential of stoichiometric UO_2 and the Cr-Cr_2O_3 equilibrium, which will be used in this study.

Figure 2 shows that the Cr-Cr_2O_3 equilibrium occurs at an oxygen potential that is commensurate with slightly hyper-stoichiometric UO_{2+x}. The reducing environment that doped fuel is sintered under makes it likely that the O/U ratio is close to 2 and the oxygen potential is close to the Cr-Cr_2O_3 equilibrium. For example, Bourgeois et al. observed both Cr metal and Cr_2O_3 oxide phases present in the same sample after sintering UO_2 doped with 0.25 wt.% Cr_2O_3 in 1 vol.% H_2O in H_2 [5].

It is our hypothesis that in Cr-doped UO_2 the oxygen potential is governed by the Cr-Cr_2O_3 equilibrium over the range of temperatures relevant to normal reactor operation (typically <1600 K). To examine this hypothesis, Thermo-Calc was used to calculate the oxygen potential of the Cr_2O_3-$UO_{2\pm x}$ system as a function of x, T, and Cr_2O_3 content. Figure 3 represents the excess oxygen in the UO_{2+x} phase at a given temperature for several different systems. Firstly, the blue line represents the case for x in UO_{2+x}, with the oxygen potential defined by the two-phase Cr-Cr_2O_3 equilibrium over the full temperature regime, showing that at low temperatures the system approaches exactly stoichiometric UO_2 ($x = 0$) and at high temperatures a peak excess oxygen value of $x = 4.6 \times 10^{-4}$ is reached. The change from $x = 0$ to $x = 4.6 \times 10^{-4}$ is below the typical accuracy for measurements of non-stoichiometry. However, such subtle changes in composition may still correspond to significant variation in the concentrations of defects that govern diffusion (as will be explored using an atomistic approach in Section 3.3). The gray vertical lines indicate the effect of varying the initial value of x in the UO_{2+x} phase. This shows that for stoichiometric UO_2 with additions of 1000 wt. ppm Cr_2O_3 the oxygen potential is gov-

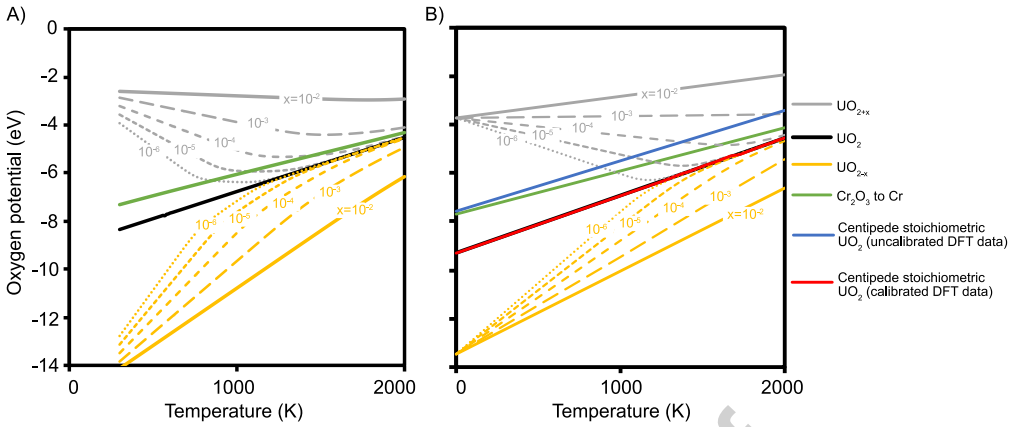

Figure 2: The oxygen potential of UO_{2+x} (gray lines), UO_2 (black line), and UO_{2-x} (yellow lines) for various values of x from A) Calphad and B) the Lindemer and Besmann [62] model. The oxygen potential of the two-phase Cr-Cr_2O_3 equilibrium is shown by the green line for A) Calphad and B) the JANAF tables. Additionally, the oxygen potential of stoichiometric UO_2 in the uncalibrated (blue) and calibrated (red) Centipede simulations are shown in B). Calibration of the point defect energies in the Centipede simulations are shown in Table 1.

erned by the Cr-Cr_2O_3 equilibrium from 300 K to 2500 K. Conversely, if the initial value of x is greater than 4.6×10^{-4} then Cr_2O_3 remains stable over the full temperature range and there is no influence of Cr-Cr_2O_3 on the oxygen potential. For $0 < x < 4.6 \times 10^{-4}$, the temperature range over which the Cr-Cr_2O_3 equilibrium dominates varies. All cases discussed so far represent the UO_2 pellet without the presence of a reducing external gas and are representative of conditions the pellet might experience in-reactor, given that the fuel rod is backfilled with inert He.

Alternatively, when sintering the doped pellets or performing diffusivity measurements, the pellets would be in equilibrium with an external gas. The dashed/colored lines in Figure 3 show the impact of varying the atom fraction of a 1 vol.% H_2O in H_2 static gas, the dopant content, and the initial value of x in the gas-Cr_2O_3-UO_{2+x} system. It can be seen that the excess oxygen is no longer governed by the Cr-Cr_2O_3 equilibrium below 1500 K for all gas fractions studied. If the system is initiated with stoichiometric UO_2, 0.01 atom fraction of a gas with composition 1 vol.% H_2O in H_2 ($\approx$ 0.06 L of gas in equilibrium with a pellet 1 cm in both diameter and height), and 1000 wt. ppm Cr_2O_3 (green line), the Cr-Cr_2O_3 equilibrium dominates from 1500 K to 2750 K. The red line indicates that inclusion of 0.50 atom fraction of gas ($\approx$ 3 L of gas in equilibrium with a pellet 1 cm in both diameter and height) results in the Cr-Cr_2O_3 equilibrium dominating from just 1950 K to 2010 K. However, the residual influence of reducing Cr_2O_3 to Cr and transferring oxygen to the UO_2 phase continues to higher temperatures, as can be seen by the difference in the "no dopant" and "1000 wt. ppm" red lines. The yellow and gray lines show the effect of modifying the initial value of x in the UO_{2+x} phase. In short, the presence of a 1 vol.% H_2O in H_2 gas has a significant influence on the range of temperatures and the way in which the dopant influences the O/U ratio of the UO_{2+x} phase.

Generally, the reactive 1 vol.% H_2O in H_2 gas can be said to limit the impact that the dopant has, making fission gas behavior sensitive to the conditions of a given furnace. However, for in-reactor conditions, the omission of a reactive gas is justified due to the backfill gas consisting of inert He and the large molar fraction of UO_2 that makes up the contents of the fuel rod.

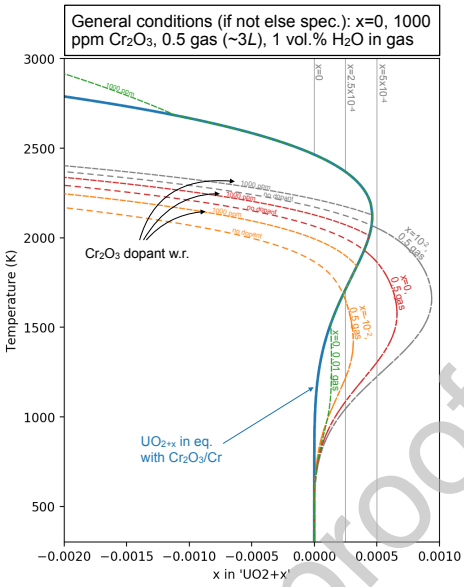

Figure 3: The excess oxygen in the UO_{2+x} phase at a given temperature (shown as $T(x)$) for several different systems. The blue line indicates x in UO_{2+x} when in equilibrium with Cr-Cr_2O_3. The vertical gray lines indicate different starting values of x, whereby their intercept with the blue line shows the temperature range over which the Cr-Cr_2O_3 equilibrium is important. The colored dashed lines indicate systems of UO_{2+x} (x = -0.01, 0.00, and 0.01) with either no dopant or 1000 ppm weight ratio (w.r.) of Cr_2O_3 and in the presence of 0.01 or 0.50 atom fraction of 1 vol.% H_2O in H_2 gas (≈0.06 L and ≈3 L of gas respectively).

Therefore, assuming an initially stoichiometric UO_2 phase with additions of 1000 wt. ppm Cr_2O_3 (vertical gray line labeled $x = 0$ in Fig. 3), it is justified to treat the oxygen potential in-reactor as governed by the Cr-Cr_2O_3 equilibrium for temperatures up to at least 1700 K. Above this temperature, it is acknowledged that Cr solubility in UO_2, which has been omitted from these calculations, may begin to influence the results in Figure 3. However, this does not impact our primary conclusion that the Cr-Cr_2O_3 equilibrium governs the oxygen potential for temperatures relevant to normal operating conditions (<1600 K).

3.2. Calibration of thermodyanmic parameters in Centipede simulations

Having identified a route through thermodynamics by which doping can influence the fission gas behavior, the thermodynamic accuracy of the DFT data used in the Centipede simulations is ascertained. The O/U ratio predicted by the Centipede simulations for a given oxygen potential and temperature is governed by the underlying oxygen point defect energies calculated from DFT and empirical potentials in Perriot et al. [37]. The oxygen interstitial and vacancy formation reactions are described by Eqs. (13) and (14), respectively. Based on the formation energies associated with these reactions, the oxygen potential at which UO_2 is exactly

stoichiometric is given by Eq. (15):

$$\frac{1}{2}O_2 + V_i^{\times} + 2U_U \xrightarrow{\Delta G_{O_i}} O_i'' + 2U_U^{\bullet} \tag{13}$$

$$O_O + 2U_U \xrightarrow{\Delta G_{V_O}} V_O^{\bullet\bullet} + 2U_U' + \frac{1}{2}O_2 \tag{14}$$

$$p^0_{O_2} = \frac{2K_{V_O}}{K_{O_i}} = 2\exp\left(\frac{-(\Delta G_{V_O} - \Delta G_{O_i})}{k_B T}\right) \tag{15}$$

where standard Kröger-Vink notation is used [64], formal defect charges are applied, ΔG_{O_i} and ΔG_{V_O} are the oxidation and reduction energies, respectively, and K_{O_i} and K_{V_O} are the corresponding reaction coefficients. Given that Frenkel disorder is dominant in UO_2, for stoichiometric UO_2, $[V_O] = [O_i]$ and the oxygen partial pressure at which UO_2 is exactly stoichiometric, $p^0_{O_2}$, can be derived, as in Eq. (15). The factor of 2 is based on the defect concentrations being defined as per UO_2 formula unit. Hence, there are two possible V_O sites per UO_2 and one O_i site.

Figure 2B shows the reference thermodynamic data for UO_2 and Cr-Cr_2O_3, alongside the oxygen potential for stoichiometric UO_2 as defined by Eq. (15) and the original DFT data (blue line) [37]. It can be seen that the oxygen potential of stoichiometric UO_2 in the original model exceeds that of the thermodynamic data from Lindemer and Besmann [62]. In fact, the oxygen potential defined by the Cr-Cr_2O_3 equilibrium, Eq. (12), is commensurate with hypo-stoichiometric UO_{2-x} in the version without alterations to the DFT data (i.e. the green line lies below the blue line). Comparison with the thermodynamic data of Lindemer and Besmann [62] indicates that driving the system into the hypo-stoichiometry regime is inaccurate. The same result is obtained using the Calphad model, as shown in Figure 2A.

There are a number of known inaccuracies in the underlying atomic scale data that could lead to a different oxygen potential for a given composition. For example, the bandgap of UO_2 is measured to be ≈2.0 eV [65], whereas the energy of the electron-hole reaction,

$$2U_U \rightarrow U_U^{\bullet} + U_U' \quad , \tag{16}$$

is 1.36 eV from LDA+U [37].

Here, we calibrate the point defect energies so that the oxygen potential for stoichiometric UO_2 in the Centipede simulations matches that given by Lindemer and Besmann [62]. While it is our intention to match the description of O/U as a function of oxygen potential and T, ideally for a given O/U and T the underlying defect concentrations will not be significantly changed compared to the original model so that the fundamental diffusion mechanisms are still correctly predicted (e.g. the importance of the $\{Xe : 4V_U : 3V_O\}$ cluster for D_2 diffusion [39]). To achieve this and due to a greater degree of confidence in stoichiometric reactions rather than oxidation and reduction reactions, the alterations made to the energies of the oxygen Frenkel, uranium Frenkel, Schottky, and anti-Schottky reactions, listed below, are minimized:

$$O_O + V_i \rightarrow V_O^{\bullet\bullet} + O_i'' \tag{17}$$

$$U_U + V_i \rightarrow V_U'''' + U_i^{\bullet\bullet\bullet\bullet} \tag{18}$$

$$U_U + 2O_O \rightarrow V_U'''' + 2V_O^{\bullet\bullet} + UO_2 \tag{19}$$

$$3V_i + UO_2 \rightarrow U_i^{\bullet\bullet\bullet\bullet} + 2O_i'' \tag{20}$$

The changes to the point defect energies and entropies are summarized in Table 1, alongside the changes to the energies and entropies of Eqs. (17) to (20). The enthalpy and entropy that

define the stoichiometric UO_2 oxygen potential (described by Eq. (15)) have been shifted by -1.73 eV and 3.46 k_B, respectively. This is demonstrated in Fig. 2 by a reduction in the intercept (enthalpy) and an increase in the gradient (entropy) of the oxygen potential of stoichiometric UO_2 in the calibrated model (red line) compared to the uncalibrated model (blue line). It can be seen from Fig. 2B that an excellent fit to the reference thermodynamic data [62] is now achieved.

Table 1: (left) Adjustments to the point defect energies and entropies used in the Centipede simulations to match the Lindemer and Besmann thermodynamic data for stoichiometric UO_2 [62]. (right) The impact of the point defect energy and entropy changes on key reactions in the Centipede simulations.

Defect	ΔH eV	ΔS (k_B)		Reaction	ΔH eV	ΔS (k_B)
O_i''	-0.44	-1.00		Oxygen Frenkel Pair, Eq. (17)	-0.10	0.00
$V_O^{\bullet\bullet}$	0.34	1.00		Uranium Frenkel Pair, Eq. (18)	0.00	0.00
V_U''''	-0.67	-2.00		Schottky Defect, Eq. (19)	0.00	0.00
$U_i^{\bullet\bullet\bullet\bullet}$	0.67	2.00		Anti Schottky Defect, Eq. (20)	-0.20	0.00
$U_U^{\bullet}$	0.14	-0.37		Electron-hole pair, Eq. (16)	0.75	0.00
U_U'	0.61	0.37		O_i formation, Eq. (13)	-0.17	-1.73
				V_O formation, Eq. (14)	1.57	1.73

A large number of clusters are also included in the cluster dynamics simulations for Xe diffusion. The cluster energies, $G_{cluster}$, have been modified to ensure that the binding energy, G_{BE}, to form the cluster from the constituent point defects, G_i, is unchanged. This restriction is enforced since there is greater confidence in the binding energies than the absolute energy of a given defect cluster. Furthermore, such clusters have no influence on the observable thermodynamic information (governed by oxygen point defects) and, thus, their absolute energies could not be reliably fitted to the reference thermodynamic data.

Having calibrated the thermodynamics of the Centipede simulations to match the reference data, it is possible to directly apply the oxygen potential of the Cr-Cr_2O_3 equilibrium to describe the oxygen potential in simulations of doped UO_2. There are a number of other uncertainties in the model relating to the kinetics of defect production and annihilation. To examine the influence of these on the fission gas diffusivity, two cases are tested: one where minimal alterations are made to the underlying DFT data (Case A), and another where the possibility that DFT overestimates the migration barrier of V_U is tested (Case B). These two cases are motivated based on experience from Matthews et al. [38]. In that paper, comparison to the experimental data of Sabioni et al. [66] for the U self-diffusivity in the intrinsic regime, showed an underestimation of one order of magnitude for the baseline case [38]. This may be explained by environmental conditions (uncertainty in the true oxygen partial pressure) or parameter uncertainty, as explored in Matthews at al. [38]. The migration barrier of the uranium vacancy was identified as one of the most influential parameters in this context [38]. Moreover, the transition between the intrinsic and irradiation-enhanced regimes occurs at a rather high temperature for both U self-diffusion [38] (1850 K) and Xe diffusion [39] (1650 K), which is mainly controlled by the uranium vacancy migration properties similar to self-diffusion. Although the arguments above are indicative rather than conclusive, we use them to motivate treating two cases for the U vacancy migration barrier: one identical to previous studies and one where the barrier is reduced by 0.34 eV (a reasonable adjustment based on typical uncertainty in DFT calculations on UO_2). In both cases, the sink and source strengths are also recalibrated to ensure a good agreement with the Turnbull model for D_2 diffusivity for Xe in UO_2. Note that there is large uncertainty in the sink and source terms of up to an order of magnitude [49, 67]. The final changes to the kinetic parameters for Case A and Case B are shown in Table 2.

Table 2: Changes to kinetic parameters in the Centipede simulations [38, 39] that govern the migration energy, E_{mig}, of V_U, the source strength, and the sink strength.

Parameter	Case A	Case B
E_{mig}, V_U	unchanged	−0.34 eV
Source strength	×0.2	×10
Sink strength	unchanged	×5

As discussed previously by Matthews et al. [38, 39], in the case of undoped UO_2 the actual oxygen potential is not well known during the measurements of Xe D_2 diffusivity. Therefore, the oxygen potential in the model is similarly fitted to ensure the predicted undoped Xe diffusivity remains close to that given by Matthews et al. [39] and the Turnbull model [23, 26], which is used for the standard UO_2 model in BISON. The oxygen potential applied for undoped UO_2 (calibrated here for Case A and B) and doped UO_2 (taken directly from the Cr_2O_3 formation energy in Chase [63]) are given by:

$$\mu_{O_2}^{undoped,\,A} = -6.50 + 12.59\,k_B T \quad \text{eV} \tag{21}$$

$$\mu_{O_2}^{undoped,\,B} = -6.10 + 10.46\,k_B T \quad \text{eV} \tag{22}$$

$$\mu_{O_2}^{doped} = -7.79 + 20.63\,k_B T \quad \text{eV} \tag{23}$$

The agreement obtained for Xe diffusivity in undoped UO_2 with the Turnbull model will be shown in Section 3.4 for Case A and Case B alongside the impact of doping on diffusivity.

3.3. Defect concentrations in Cr_2O_3-doped UO_2

At high temperatures, the oxygen potential of doped UO_2 is greater (more oxidizing) than in undoped UO_2, and, at low temperatures, the oxygen potential of doped UO_2 is lower (more reducing). In previous work [37, 39], it was shown that the defect clusters important for Xe diffusion are $\{Xe : 2V_U : V_O\}$ for intrinsic diffusion and $\{Xe : 4V_U : 3V_O\}$ for irradiation-enhanced diffusion. As building blocks that affect the concentrations of these larger clusters, the concentrations of the V_U and V_O point defects are critical in governing the fission gas diffusivity. Figure 4 shows the concentrations of the V_U and V_O point defects for the undoped UO_2 and Cr-doped UO_2 oxygen potentials for Case A and Case B.

At high temperatures, both V_U and V_O are in thermal equilibrium and, as such, their concentrations are sensitive to changes in the oxygen potential. It can be seen that the increase in oxygen potential at high temperatures due to doping results in more oxidizing conditions and, therefore, an increase in the hyper-stoichiometric V_U defect concentration and a suppression of the hypo-stoichiometric V_O defect concentration.

At low temepratures, where doping lowers the oxygen potential, the thermal equilibrium concentrations of V_U and V_O are suppressed and enhanced, respectively. However, the concentration of V_U in the D_2 regime is dominated by irradiation processes and is, thus, independent of the dopant-induced oxygen potential. Conversely, V_O is as assumed to be in thermal equilibrium, given that their high mobility ensures that any defects generated by irradiation are rapidly eliminated through mutual recombination and interaction with sinks. Therefore, in the irradiation-enhanced regime, there is an increase in V_O due to doping, while the V_U concentration is unaffected. As discussed in previous work [38, 39], the mobile $\{U_i : 2O_i\}$ cluster plays an important role in the concentrations of larger vacancy clusters, as it can annihilate and reduce their concentration. It can be seen in Fig. 4 that the oxygen potential has a limited

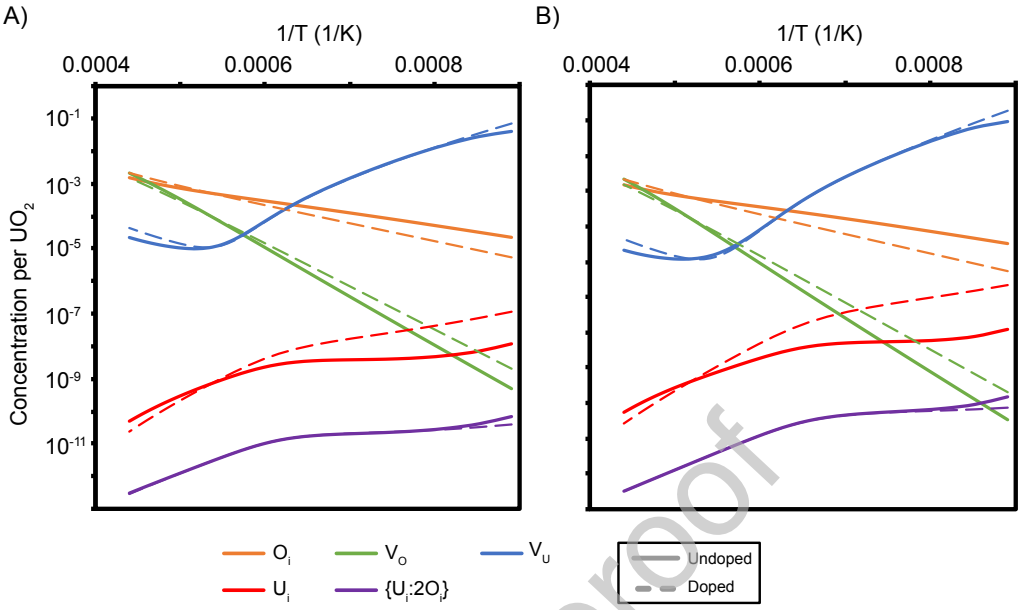

Figure 4: The concentrations of the V_U, V_O, O_i, U_i, and $\{U_i 2O_i\}$ defects predicted under irradiation for Case A and B for undoped UO_2 (solid lines), and doped UO_2 (dashed lines). V_O and O_i are always at thermal equilibrium and are unaffected by irradiation, whereas uranium-type defect concentrations are influenced by irradiation.

impact on the concentration of $\{U_i : 2O_i\}$, given that it is a stoichiometric defect. Conversely, the more reducing conditions increase the concentration of the hypo-stoichiometric U_i defect at low temperatures. While the above discussion applies to both Case A and Case B, the trends are more pronounced for Case B.

Changes to the point defect concentrations due to doping will have an impact on the concentrations of all larger clusters in the system that are composed of those point defects. Figure 5 shows the concentrations of a selection of the clusters considered in the Centipede simulations. Importantly, the concentrations of the two clusters that dominate Xe diffusion, $\{Xe : 2V_U : V_O\}$ (D_1) and $\{Xe : 4V_U : 3V_O\}$ (D_2), are enhanced by doping. This is due to the more oxidizing conditions at high temperatures and more reducing conditions at low temperatures induced by Cr doping. For $\{Xe : 2V_U : V_O\}$, the enhancement at high temperatures is due to the enhanced V_U concentration, which favors $\{Xe : 2V_U : V_O\}$ over the dominant $\{Xe : V_U : V_O\}$ cluster through the $\{Xe : V_U : V_O\} + V_U \rightarrow \{Xe : 2V_U : V_O\}$ reaction. Although V_O concentrations are lower in this regime, there is no influence on the equilibrium of this reaction as both clusters involved have the same number of V_O defects.

In the D_2 regime, the concentration of V_U is unaffected by doping, despite the more reducing conditions. Similarly, the $\{U_i : 2O_i\}$ concentration is unchanged. These two defects are critical in governing the accumulation of point defects to form the large clusters responsible for diffusion, and would at first glance indicate little change in behavior due to doping. However, the increase in the V_O concentration causes the $\{Xe : 4V_U : 3V_O\}$ cluster to also increase in concentration. Otherwise, in undoped UO_2 the $\{Xe : 4V_U : 2V_O\}$ cluster dominates. This is due to the increased

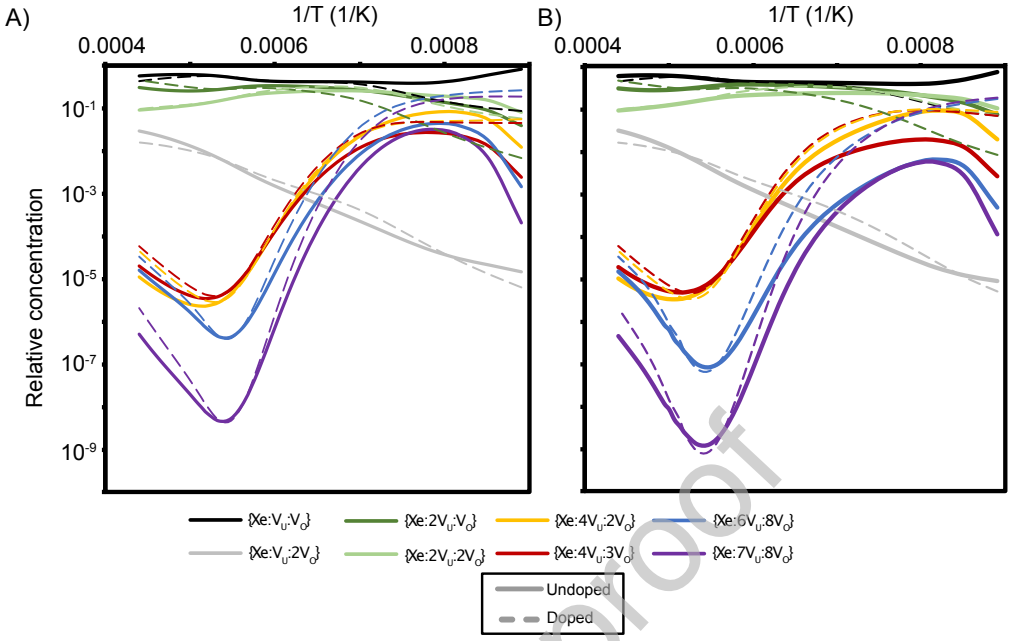

Figure 5: The defect concentrations of a range of Xe-bearing clusters predicted by cluster dynamics simulations for Case A and Case B for undoped UO_2 (solid lines), and doped UO_2 (dashed lines) under irradiation. For clarity this represents a subset of clusters considered.

relative stability of $\{Xe:4V_U:3V_O\}$ compared to $\{Xe:4V_U:2V_O\}$ under the more oxygen-poor conditions induced by Cr-doping. This is important for fission gas diffusivity, given the finding of Matthews et al. that the more mobile $\{Xe:4V_U:3V_O\}$ cluster is responsible for irradiation-enhanced diffusivity [39]. As for the host defects discussed previously, the trends for Case A and B are similar but are more pronounced for Case B.

3.4. Fission gas diffusivity in Cr_2O_3-doped UO_2

Having calculated the change in the concentration of all defect clusters in the system due to doping, the total Xe diffusivity can be calculated as:

$$D = \frac{\sum_i x_i D_i}{\sum_i x_i} \tag{24}$$

where D_i and x_i are the diffusivity and concentration of a given cluster, i, and $\sum_i x_i$ fulfills the total Xe concentration. The concentrations of a select number of clusters were shown previously in Fig. 5. The diffusivities of all clusters are determined and summed in Eq. (24) to give the total Xe diffusivity, as shown in Fig. 6 for undoped UO_2 and doped UO_2 by the solid and dashed black lines, respectively. As discussed previously in Section 3.3, there is uncertainty regarding the oxygen potential in the experimental setups used to measure the fission gas diffusivity. As such, when comparing to the standard model for undoped UO_2 (the Turnbull model), which was derived from these experiments, the oxygen potential (see Eqs. (21) and (22)) and the sink and source strengths (see Table 2) in the Centipede simulations are calibrated to achieve a reasonable agreement in the D_2 regime, given its dominance at reactor operating temperatures

(as shown in Fig. 6). For both Case A and B, a good agreement is obtained for the diffusivity in undoped UO_2 compared to the Turnbull model, particularly in the range where the cluster dynamics simulations remain within the point defect limit (delineated by the vertical black lines in Figure 6).

The enhancement in the relative concentration of $\{Xe : 2V_U : V_O\}$ due to doping, shown in Fig. 5, translates directly to an increase in the Xe diffusivity for the intrinsic D_1 diffusion regime, as shown in Fig. 6. Similarly, the increase in the relative concentration of $\{Xe : 4V_U : 3V_O\}$ results in greater Xe diffusivity in the irradiation-enhanced D_2 diffusion regime. Enhanced D_1 diffusion is in qualitative agreement with the observations made by Kashibe and Une for out-of-pile experiments [24]. However, the Centipede simulations, while in good agreement with the Turnbull model [23], predicts Xe diffusivity to be over one order of magnitude greater than the data from Kashibe and Une (shown in Fig. 1) for both undoped and doped UO_2. This is likely due to variation in the oxygen potential between the Kashibe and Une experiments, as compared to that used in our model and in the experiments used to derive the Turnbull model. The Centipede results presented here provide evidence that the irradiation-enhanced D_2 diffusivity is also enhanced by Cr doping. This is particularly for D_2 diffusion, which is dominant for the temperatures experienced by the pellet in-reactor.

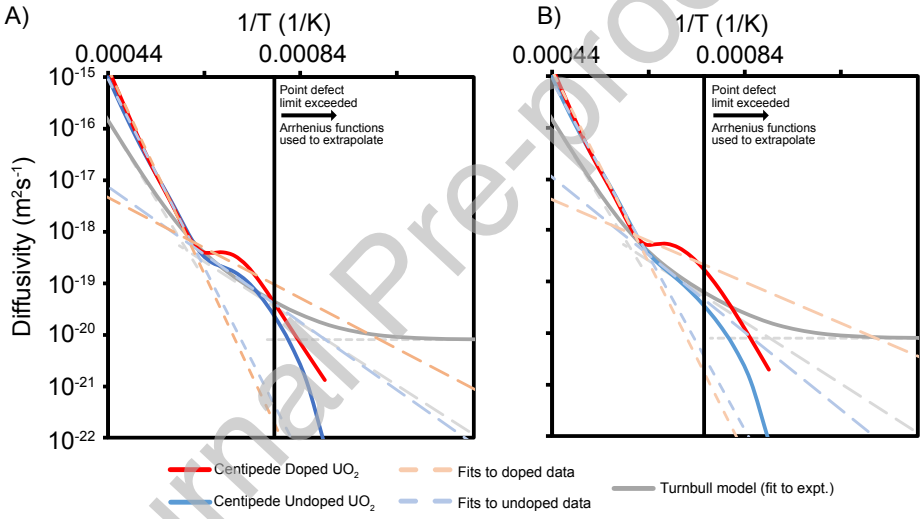

Figure 6: The Xe diffusivity predicted from cluster dynamics simulations for doped and undoped UO_2. The Turnbull model for undoped UO_2 is included for comparison. A) and B) correspond to Case A and B, respectively, as also shown in Table 2. The Arrhenius fits to the Centipede simulation results that were used to derive the parameters for Eq. (25) are shown by dashed lines (also see Table 3).

3.5. Analytical expressions for use in BISON

Solving the full set of ODEs is too computationally challenging and time consuming to be directly implemented into a fuel performance code, such as BISON. To enable the application of our predictions in the FGR model in BISON, for Case A and B, four Arrhenius functions (shown by dashed lines in Fig. 6) have been fitted to four regimes: i) D_1 undoped, ii) D_1 doped, iii) D_2 undoped, and iv) D_2 doped. The functions were not fitted to Centipede simulations results

below 1275 K (Case A) and 1325 K (Case B) because the uranium vacancy concentrations began to exceed 1% and the dilute limit assumption broke down, making the predictions less reliable. The four Arrhenius functions have been reformulated into a single expression for each case that describes the enhancement in Xe diffusivity, relative to the baseline undoped UO_2 model, as follows:

$$D^{doped} = \exp\left(-\frac{\Delta H_1}{k_B}\left[\frac{1}{T}-\frac{1}{T_1}\right]\right)D_1^{undoped} + \exp\left(-\frac{\Delta H_2}{k_B}\left[\frac{1}{T}-\frac{1}{T_2}\right]\right)D_2^{undoped} + D_3^{undoped} \tag{25}$$

where the parameters T_1, T_2, ΔH_1, and ΔH_2 are reported in Table 3 for Case A and Case B.

Table 3: Parameters for the multiscale analytical enhanced diffusivity models derived for Cr-doped UO_2, see Eq. (25).

Parameter	Case A	Case B
$T_1 = T_2$ (K)	1773	1773
ΔH_1 (eV)	0.3198	0.3282
ΔH_2 (eV)	-0.3345	-0.6998

Figure 7 shows the result of applying Eq. (25) to D_1, D_2, and D_3 from the standard empirical model of Xe diffusivity in undoped UO_2 used in BISON (see Eqs. (8) to (11)). It can be seen from Fig. 7 that the unperturbed Xe diffusivity in doped UO_2 (D^{doped}) is enhanced in both the high temperature D_1 and lower temperature D_2 regimes, as expected from Fig. 6. Case B (assuming a lower V_U migration energy) indicates greater enhancement in D_2 diffusivity than Case A.

To estimate the effective diffusivity, the intra-granular bubble radius and number density, R and N in Eqs. (6) and (7), must be provided. While BISON explicitly evolves N and R during the simulation [50], for the purposes of plotting the effective diffusivity in Fig. 7, the following correlations from White and Tucker are used [49]:

$$R = 5\times10^{-10}(1+106\cdot\exp(-8691.6/T)) \quad \text{m} \tag{26}$$

$$N = \frac{1.52\times10^{27}}{T} - 3.3\times10^{23} \quad \text{bubbles}\cdot\text{m}^{-3} \tag{27}$$

The effective diffusivity is shown as a function of T by the dashed lines in Fig. 7. It can be seen that doping results in a significantly enhanced effective diffusivity at temperatures dominated by the irradiation-enhanced intra-granular diffusivity of Xe, thus emphasizing the importance of the FECD treatment of irradiation effects carried out in previous sections. At high temperatures where intrinsic (D_1) diffusivity dominates, there is no impact of doping on the effective diffusivity because it is already at its maximum value, as defined by $b/(4\pi RN)$ (see Eqs. (5) to (7)).

These three different diffusivity models (undoped, Case A, and Case B) will be evaluated against experimental FGR studies, as follows: Section 3.6 compares the model to experiments conducted in the Halden reactor and Section 3.7 compares the models to experiments conducted by the Commissariat à l'énergie atomique et aux énergies alternatives (CEA) and Framatome (formerly known as AREVA).

3.6. Modeling fission gas release during IFA-716.1 Halden experiments

Carried out between January 2011 and May 2015, the IFA-716.1 experiment investigated the FGR, swelling, and densification behavior of Cr_2O_3-doped fuel and large-grained UO_2 fuel by irradiating six rods in the Halden reactor [52, 68]. Initially, the rods were irradiated for 12 cycles

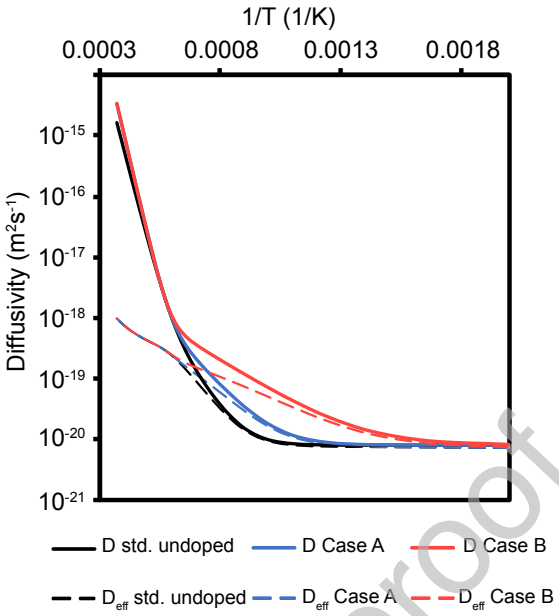

Figure 7: The Xe diffusivity in Cr-doped UO_2 predicted by applying Eq. (25) to the standard empirical undoped UO_2 diffusivity in BISON. Solid lines show the unperturbed diffusivity and the dashed lines show the resultant effective diffusivity, once trapping and resolution has been included using Eq. (5).

and subsequently were reloaded for 3 more cycles. Two of the rods contained Cr_2O_3-doped UO_2, supplied by Framatome, and are suitable as validation cases for the fission gas diffusivity models for doped UO_2 developed in this work. The plenum pressure and fuel temperature were measured in-situ by the pressure transducers and fuel centerline thermocouples equipped on each one of the rods. For each rod, the thermocouple was placed in the drilled section at the top of the fuel stack. The evolution of fractional fission gas release was estimated from normalized pressure, and rod 6 was punctured at the end of life providing a more accurate FGR estimation.

Integral simulations of the Cr_2O_3-doped fuel rods in the Halden IFA-716.1 test were performed with the BISON code, using the doped UO_2 material models outlined in Section 2.2. Several different variations of the fission gas diffusivity were evaluated for fuel behavior during Halden tests (see Figs. 8 to 10): i) the standard UO_2 empirical (Turnbull) model (blue lines), ii) Case A (solid black lines), and iii) Case B (dashed black lines) of the lower length scale (LLS) informed diffusivity model developed in this work. For the empirical undoped UO_2 (Turnbull) model, a smaller (5.5 μm) grain radius, typical of undoped UO_2, was tested in addition to the large grains reported in Table 4 that pertain to the actual fuel in the simulated experiments. This was done in order to investigate the effect of the grain size on FGR in the calculations. For all other diffusivity cases, only the large grain size was used.

Figure 8 shows the measured upper centerline thermocouple temperature from the Halden tests for rods 1 and 6 (red lines), alongside BISON predictions of the temperatures at the same position using the different diffusivity models. All diffusivity models show a similar agreement with the measured data. Regardless of the diffusivity model selected, there is a significant over-estimate of the centerline temperature during the later irradiation cycles. It is worth not-

Table 4: Fabrication characteristics of IFA-716.1 rod 1 and 6 simulated in this work [52, 68].

	IFA-716.1 Rod 1	IFA-716.1 Rod 6
Cladding material	Zircaloy-4	Zircaloy-4
Fuel material	UO_2+Cr_2O_3	UO_2+Cr_2O_3
Fill gas	He	He
Total active fuel stack length (mm)	399.5	399.3
Drilled active section length, top (mm)	110	110
Drilled active section length, bottom (mm)	-	-
Pellet inner diameter, drilled sections (mm)	1.8	1.8
Pellet outer diameter (mm)	9.12	9.12
Diametral gap (μm)	180	180
Cladding thickness (mm)	0.725	0.725
Cladding outer diameter (mm)	10.75	10.75
Free volume (cm^3)	5.80	6.0
Fill gas pressure (MPa)	1	1
Fuel Cr_2O_3 content (ppm)	1580	1050
Fuel U-235 enrichment (%)	4.9	4.89
Initial fuel density (kg/m^3)	10500	10530
Fuel average grain radius (μm)	35	29.5

ing that independent calculations with the ALCYONE fuel performance code for IFA-716.1 rod 6 [69] have led to similar results in terms of an over-estimate of the fuel centerline temperature during the later irradiation cycles. The fact that independent calculations showed this behavior may indicate that the linear heat rate (LHR) provided by the Halden Project, which form the basis for the input LHR histories used in the calculations, are affected by inaccuracies during the later portion of the irradiation. Indeed, this issue has been postulated for other Halden tests such as IFA-677, with inaccuracies in the power data potentially arising following a core configuration change, the effect of which is not taken into account in the power distribution reconstruction [70, 71]. This may have occurred also for IFA-716.1, for example following temporary rig unloadings from the core, which were performed during periods where excess reactor power was expected [52]. Additionally, in general, there is an uncertainty of at least 7 % in the LHR data. To this end, the fuel centerline temperature is roughly proportional to the local LHR.

Figure 9 shows the comparison of the measured plenum pressure and BISON predictions using different diffusivity models. The pressure transducer on rod 1 failed after around 625 irradiation days [52]. For this reason, the measured plenum pressure data after that time is not meaningful, and has been omitted from Fig. 9a. The standard UO_2 diffusivity with standard UO_2 grain sizes (5.5 μm) model severely overestimates the plenum pressure because of substantial FGR. On the other hand, using the standard empirical UO_2 diffusivity model together with the actual larger grain size underestimates the plenum pressure due to excessively suppressed FGR. This result clearly demonstrates the benefits of large grains for fission gas retention without any considerations for the impact of doping on fission gas diffusivity. Case A and Case B both include the impact of enhanced fission gas diffusivity informed from LLS techniques in Section 3.4 and the large grain size reported in Table 4. As a result, both LLS-informed cases provide more accurate predictions of the plenum pressure, with Case A matching better with experimental data for rod 1 and Case B performing better for rod 6.

The FGR as a function of burnup for the IFA-716.1 test is shown in Figure 10. The online measurement of FGR was estimated from the rod pressure assuming that no FGR occurs

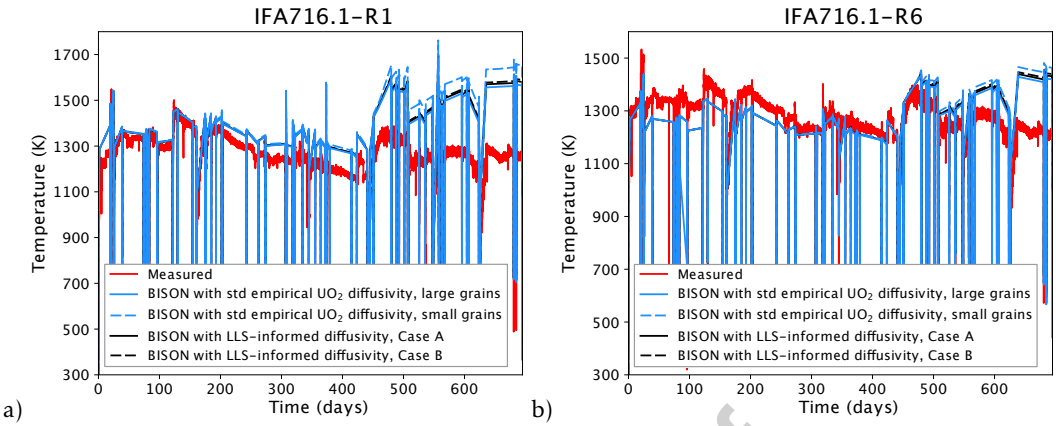

Figure 8: The upper thermocouple temperature measured during the IFA-716.1 test on Cr_2O_3-doped fuel (red lines) for a) rod 1 and b) rod 6 [52]. The BISON results using the LLS-informed enhanced diffusivity model developed in this work are shown by the black lines for Case A and Case B. Comparison is made to results using the standard empirical undoped UO_2 model with small and large grains (blue lines).

until the power uprate [52]. This assumption may partly explain the discrepancies between the burnups at the onset of FGR for the measured and calculated data. Due to the failure of the pressure transducer in rod 1 at around 625 irradiation days [52], the measured on-line FGR is cut-off similarly to the pressure data shown previously. It can be clearly seen that, by applying the standard empirical undoped UO_2 diffusivity model, there is poor agreement with the measured data for both rods: if large grains are used, there is a tendency to under-estimate the FGR; and, if small grains are used, it is greatly over-estimated. As expected, by applying the LLS-informed enhanced diffusivity models derived in this work there is an increase in the FGR with respect to the baseline empirical undoped UO_2 model. Both Cases A and B provide reasonable agreement with the Halden tests. In particular, there is excellent agreement between the predicted and the measured FGR data for rod 6.

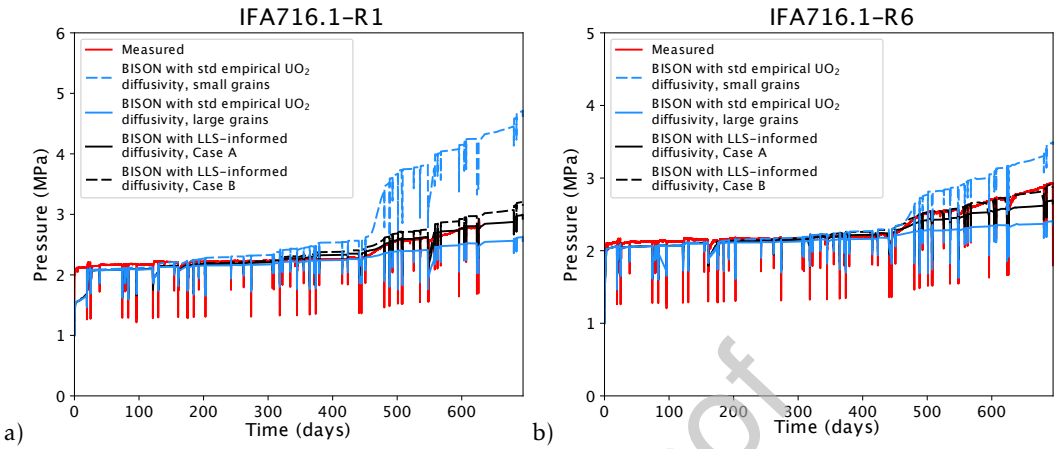

Figure 9: The pressure measured during the IFA-716.1 test on Cr_2O_3-doped fuel (red lines) for a) rod 1 and b) rod 6 [52]. The BISON results using the LLS-informed enhanced diffusivity model developed in this work are shown by the black line for Case A and Case B. Comparison is made to results using the standard empirical undoped UO_2 model with small and large grains (blue lines).

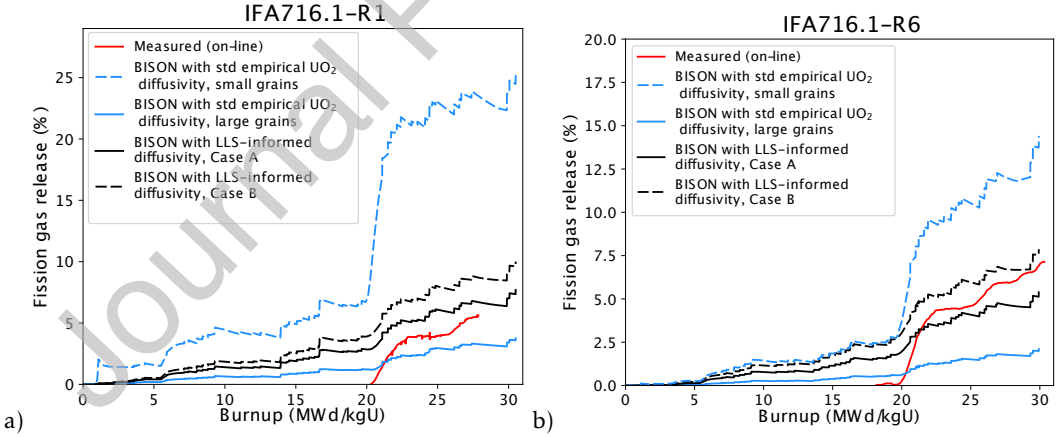

Figure 10: The measured FGR (inferred from rod pressure) during the IFA-716.1 test on Cr_2O_3-doped fuel (red lines) for a) rod 1 and b) rod 6 [52]. The BISON results using the LLS-informed enhanced diffusivity model developed in this work are shown by the black lines for Case A and Case B. Comparison is made to results using the standard empirical undoped UO_2 model with small and large grains (blue lines).

3.7. Modeling transient fission gas release during Framatome experiments

A series of ramp tests were performed by Framatome between late-2000 and mid-2005 in the Dampiere 1 pressurized water reactor (PWR). Three of the rodlets in assembly FX13AW used UO_2 fuels with the additive Cr_2O_3, and they are identified as K14-2, N07-2 and G04-2 according to their rod position and segment number. Rodlets K14-2 and N07-2 went through two cycles of base-irradiation in the Dampiere 1 reactor before being removed for ramp tests in the ISABELLE 1 test loop in the OSIRIS reactor at Saclay, France. Rodlet G04-2 experienced a more complicated power history. For benchmarking purposes in this work, only K14-2 and N07-2 are modeled in BISON.

Framatome benchmarked the ramp tests in BISON using the empirical Che et al. methodology [22] for K14-2 and N07-02 using BISON. For the two ramped tests, the ratio of predicted FGR over the measured FGR at the end of the power ramp was 0.77 (K14-2) and 0.91 (N07-02). The measured FGR in Framatome ramp tests are proprietary, and thus no absolute values are given here. Since Framatome did not have access to the new diffusivity models developed in this work at the time the validation work was completed, we first reran BISON with the Che et al. model [22] with non-proprietary available information on K14-2 and N07-02 ramp tests.

An initial base irradiation in a PWR with a constant power level of 25 kW/m was modeled in BISON, reaching a burnup level of 29.7 MWd/kgU and 29.9 MWd/kgU for rodlets K14-2 and N07-2, respectively, at the end of the base irradiation. A subsequent pause in power history was inserted to simulate the transfer from the PWR to the test loop. During the ramp test, rodlet K14-2 (N07-2) was conditioned at ~22 kW/m (~21 kW/m) for 14 hours, followed by a power ramp to ~47 kW/m (~50 kW/m), and eventually held at this terminal power for 12 hours. The same version of BISON was used in our reproduction of the Framatome simulation for consistency, and the reproduced average fuel temperatures are compared to the Framatome results in Table 5.

Table 5: BISON simulated average fuel temperature by Framatome and reproduced results using the Che et al. model [22].

	K14-02 temperatures (K)		N07-02 temperatures (K)	
	Conditioning phase	Holding phase	Conditioning phase	Holding phase
Framatome	917.15	1363.15	923.15	1514.15
Reproduced	917.10	1363.32	922.85	1508.88

As listed in Table 5, the predicted average fuel temperatures are very close to the Framatome results during both the conditioning and holding phases. The average fuel temperature during the holding phase for N07-02 is slightly underestimated by around 5 K, which is not expected to significantly impact the FGR at the end of a power ramp. Then, we applied the same diffusivity models as described in Section 3.6 in BISON to compare to the Che et al. model [22], with the FGR prediction at the end of the power ramps shown in Table 6. The back-calculated FGRs are used as an approximation of the measured FGR based on the ratio given by the Framatome validation work, as shown Table 6. For both rodlets, the LLS-informed Case A model offers similar predictions to the results of the empirical Che et al. model [22], in line with the performance for the Cr_2O_3-doped fuel Halden test IFA-716.1. Table 6 also includes results if only the grain size is changed for the BISON's standard FGR model. As listed, the standard UO_2 empirical diffusivity model either overestimates the FGR by nearly a factor of 3 if standard (5.5 μm) grains are assumed, or underestimates FGR by a factor of 2-4 if large grains are accounted for. Similarly to comparison with the Halden experiments, this indicates that fission gas diffusivity is underestimated by using the standard UO_2 model. It is noteworthy that Case B tends to overestimate the

FGR at the end of power ramps, while its superiority maintains to standard empirical UO_2 diffusivities that either severely underestimate or overestimate the FGR for large or normal grain sizes. The ability of the LLS-informed models (particularly Case A) to reproduce the transient test results, with a mechanistic description of the underlying processes, provides confidence in the physical robustness of the fission gas behavior model for doped UO_2.

Table 6: The relative FGR (calculated divided by measured) at the end of Framatome ramp tests of Cr-doped UO_2, with different assumptions on UO_2 diffusivity in BISON.

Rodlet	Che et al. [22] model*	Std. UO_2 (small grain)	Std. UO_2 (large grain)	LLS-informed Case A	LLS-informed Case B
K14-2	0.77	2.83	0.25	0.79	1.76
N07-2	0.91	2.88	0.45	0.95	1.46

*Only this column represents actual comparison with Framatome data; other columns are subject to uncertainty in the reproduction of Framatome simulation results shown in Table 5.

4. Conclusions

The doping of UO_2 with Cr_2O_3 is designed to increase grain size during fabrication. One of the anticipated benefits of large grains is the reduction of fission gas release by extending the rate limiting intra-granular diffusion step. Another key parameter in fission gas release is the Xe diffusivity, which may be sensitive to the impact of doping on the $UO_{2\pm x}$ chemistry. In this work, using a thermodynamic investigation, we show that the oxygen potential of stoichiometric UO_2 doped with 1000 wt. ppm Cr_2O_3 is controlled by the Cr-Cr_2O_3 two-phase equilibrium below 2500 K. On that basis, we have adapted a cluster dynamics model for D_1 and D_2 Xe diffusivity in undoped UO_2, developed by Matthews et al. [38, 39], to study the impact that changes in the oxygen potential, due to doping, have on Xe diffusion. The DFT point defect energies used within the cluster dynamics simulations were calibrated to reproduce the oxygen potential of stoichiometric UO_2 defined by Lindemer and Besmann [62]. By then using the Cr-Cr_2O_3 equilibrium oxygen potential as the dominant oxygen buffer reaction in doped UO_2 and input to the calibrated cluster dynamics simulations, enhanced Xe diffusivity was predicted for D_1 and D_2 as a consequence of doping. At high temperatures (D_1), the more oxidizing conditions resulted in an enhancement in the concentration of V_U leading to stabilization of the mobile $\{Xe:2V_U:V_O\}$ cluster. At lower temperatures (D_2), the V_U concentration was unaffected by the oxygen potential, as it is governed by irradiation processes. Conversely, the V_O concentration was enhanced due to the more reducing conditions introduced through doping. This resulted in an increase in the concentrations of several larger Xe-bearing clusters, in particular the $\{Xe:4V_U:3V_O\}$ cluster that controls irradiation-enhanced D_2 diffusion.

An analytical expression that describes the predicted enhancement in Xe diffusivity due to doping has been derived and implemented in BISON. Simulations of fission gas release using the new model in BISON have been validated through integral analyses of the Halden fuel rod tests on Cr_2O_3-doped UO_2 in IFA-716.1, achieving good agreement. A comparison has also been made to the results of Framatome simulations of power ramp tests, indicating an improvement in the predictions when using the new mulitscale diffusivity model. In summary, for both the steady-state and transient conditions, the lower length scale informed models of enhanced fission gas diffusivity derived in this work compare well against the available data and, in particular, greatly improve upon the standard empirical model for undoped UO_2. The results support the idea that the impact of both large grains and enhanced fission gas diffusivity must be accounted for within the mechanistic model of fission gas release to accurately

capture the in-reactor performance of doped UO_2. The work also provides motivation for the utilization of multiscale modeling to assess the performance of other advanced fuels in support of accelerated fuel development.

Acknowledgments

Funding for this work was provided by the US Department of Energy, Office of Nuclear Energy NEAMS (Nuclear Energy Advanced Modeling and Simulation) and CASL (Consortium for Advanced Simulation of Light Water Reactors) programs. Los Alamos National Laboratory, an affirmative action/equal opportunity employer, is operated by Triad National Security, LLC, for the National Nuclear Security Administration of the U.S. Department of Energy under Contract No. 89233218CNA000001. The submitted manuscript has been authored by contractors of the US Government under Contracts DE-AC07-05ID14517, DE-NE0008416, and DE-NE0008752. Accordingly, the US Government retains a non-exclusive, royalty free license to publish or reproduce the published form of this contribution, or allow others to do so, for US Government purposes.

References

[1] International Atomic Energy Agency. Thermophysical properties database of materials for light water reactors and heavy water reactors. Technical Report IAEA TECDOC Series No. 1496, June, 2006.

[2] J. T. White, A. T. Nelson, J. T. Dunwoody, D. D. Byler, D. J. Safarik, and K. J. Mcclellan. Thermophysical properties of U_3Si_2 to 1773 K. *Journal of Nuclear Materials*, 464:275–280, 2015.

[3] J. Arborelius, K. Backman, L. Hallstadius, M. Limbäck, B. Rebensdorff, G. Zhou, K. Kitano, and R. Löfström. Advanced doped UO_2 pellets in LWR applications. *Journal of Nuclear Science and Technology*, 43:967–976, 2006.

[4] J. C. Killeen. Fission gas release and swelling in UO_2 doped with Cr_2O_3. *Journal of Nuclear Materials*, 88:177–184, 1980.

[5] L. Bourgeois, Ph. Dehaudt, C. Lemaignan, and A. Hammou. Factors governing microstructure development of Cr_2O_3-doped UO_2 during sintering. *Journal of Nuclear Materials*, 297:313–326, 2001.

[6] H. Assmann, W. Dörr, G. Gradel, G. Maier, and M. Peehs. Doping UO_2 with niobia - beneficial or not?. *Journal of Nuclear Materials*, 98:216–220, 1981.

[7] T. Fujino, T. Shiratori, N. Sato, K. Fukuda, K. Yamada, and H. Serizawa. Post-irradiation examination of high burnup Mg doped UO_2 in comparison with undoped UO_2, Mg–Nb doped UO_2 and Ti doped UO_2. *Journal of Nuclear Materials*, 297:176–205, 2001.

[8] T. Fujino, S. Nakama, N. Sato, K. Yamada, K. Fukuda, H. Serizawa, T. Shiratori. Solubility of magnesium in uranium dioxide. *Journal of Nuclear Materials*, 246:150–157, 1997.

[9] J. B. Ainscough, F. Rigby, and S. C. Osborn, The effect of titania on grain growth and densification of sintered UO_2. *Journal of Nuclear Materials*, 52:191–203, 1974.

[10] M. H. A. Piro, D. Sunderland, S. Livingstone, J. Sercombe, W. Revie, A. Quastel, K. A. Terrani, C. Judge. A review of pellet-clad interaction behavior in zirconium alloy fuel cladding. *In Reference Module in Materials Science and Materials Engineering, S. Hashmi (Ed.), Elsevier*, 1–68, 2017.

[11] T. Cardinaels, K. Govers, B. Vos, S. Van Den Berghe, M. Verwerft, L. De Tollenaere, G. Maier, and C. Delafoy. Chromia doped UO_2 fuel: Investigation of the lattice parameter. *Journal of Nuclear Materials*, 424:252–260, 2012.

[12] A. Leenaers. On the solubility of chromium sesquioxide in uranium dioxide fuel. *Journal of Nuclear Materials*, 317:62–68, 2003.

[13] M. Oguma. Microstructure effects on fracture strength of UO_2 fuel pellets. *Journal of Nuclear Science and Technology*, 19:1005–1014, 1982.

[14] C. Delafoy and P. Dewes. AREVA NP new UO_2 fuel development and qualification for LWRs applications. In *Top fuel 2006 International Meeting on LWR Fuel Performance "Nuclear Fuel: Addressing the future,"* Salamanca, Spain, October, 142–146, 2006.

[15] K. Backman, L. Hallstadius, and G. Rönnberg. Westinghouse advanced doped pellet - characteristics and irradiation behaviour. In *Advanced fuel pellet materials and fuel rod design for water cooled reactors, proceedings of a technical committee meeting*, Technical Report. International Atomic Energy Agency, IAEA-TECDOC-1654, Villigen, Switzerland, 23-26 November, 2009.

[16] G. Pastore. *Modelling of Fission Gas Swelling and Release in Oxide Nuclear Fuel and Application to the TRANSURANUS Code*. PhD thesis, Politecnicio di Milano, Milan, Italy 2012.

[17] G. Pastore, L. Luzzi, V. Marcello, and P. Van Uffelen. Physics-based modelling of fission gas swelling and release in UO_2 applied to integral fuel rod analysis. *Nuclear Engineering and Design*, 256:75–86, 2013.

[18] G. Pastore, L. P. Swiler, J. D. Hales, S. R. Novascone, D. M. Perez, B. W. Spencer, L. Luzzi, P. Van Uffelen, and R. L. Williamson. Uncertainty and sensitivity analysis of fission gas behavior in engineering-scale fuel modeling. *Journal of Nuclear Materials*, 456:398–408, 2015.

[19] J. D. Hales, R. L. Williamson, S. R. Novascone, G. Pastore, B. W. Spencer, D. S. Stafford, K. A. Gamble, D. M. Perez, R. J. Gardner, W. Liu, J. Galloway, C. Matthews, C. Unal, and N. Carlson. BISON Theory Manual The Equations Behind Nuclear Fuel Analysis. INL/EXT-13-29930 Rev. 3. Technical report, Idaho National Laboratory, Idaho Falls, USA, 2013.

[20] M. V. Speight. A Calculation on the Migration of Fission Gas in Material Exhibiting Precipitation and Re-solution of Gas Atoms Under Irradiation. *Nuclear Science and Engineering*, 37:180–185, 1969.

[21] G. Pastore, D. Pizzocri, C. Rabiti, T. Barani, P. Van Uffelen, and L. Luzzi. An effective numerical algorithm for intra-granular fi ssion gas release during non-equilibrium trapping and resolution. *Journal of Nuclear Materials*, 509:687–699, 2018.

[22] Y. Che, G. Pastore, J. Hales, and K. Shirvan. Modeling of Cr_2O_3-doped UO_2 as a near-term accident tolerant fuel for LWRs using the BISON code. *Nuclear Engineering and Design*, 337:271–278, 2018.

[23] J. A. Turnbull, C. A. Friskney, J. R. Findlay, F. A. Johnson, and A. J. Walter. The diffusion coefficients of gaseous and volatile species during the irradiation of uranium dioxide. *Journal of Nuclear Materials*, 107:168–184, 1982.

[24] S. Kashibe and K. Une. Effect of additives (Cr_2O_3, Al_2O_3, SiO_2 , MgO) on diffusional release of ^{133}Xe from UO_2 fuels. *Journal of Nuclear Materials*, 254:234–242, 1998.

[25] D. Davies and G. Long. AERE Rep. No. 4347. Technical Report. Atomic Energy Research Establishment, Harwell, UK, 1963.

[26] J. A. Turnbull, R. T. White, and C. Wise. The Diffusion Coefficient for Fission Gas Atoms in Uranium Dioxide. In *Water Reactor Fuel Element Computer Modeling in Steady State, transient and accident conditions*, Proceedings of a technical committee meeting organized by the International Atomic Energy Agency, 174–181, Preston, UK, 18-22 September, 1988.

[27] R. A. Jackson and C. R. A. Catlow. Trapping and solution of fission Xe in UO_2: Part 1. Single gas atoms and solution from underpressurized bubbles. *Journal of Nuclear Materials*, 127:161–166, 1985.

[28] R. A. Jackson and C. R. A. Catlow. Trapping and Solution of Fission Xe in UO_2. Part 2. Solution from Small Overpressurised Bubbles. *Journal of Nuclear Materials*, 127:167–169, 1985.

[29] X. Y. Liu, B. P. Uberuaga, D. A. Andersson, C. R. Stanek, and K. E. Sickafus. Mechanism for transient migration of xenon in UO_2. *Applied Physics Letters*, 98:151902, 2011.

[30] A. Thompson and C. Wolverton. First-principles study of noble gas impurities and defects in UO_2. *Physical Review B*, 84:1–11, 2011.

[31] M. W. D. Cooper, N. Kuganathan, P. A. Burr, M. J. D. Rushton, R. W. Grimes, C. R. Stanek, and D. A. Andersson. Development of Xe and Kr empirical potentials for CeO_2, ThO_2, UO_2 and PuO_2, combining DFT with high temperature MD. *Journal of Physics Condensed Matter*, 28:405401, 2016.

[32] D. A. Andersson, P. Garcia, X.-Y. Liu, G. Pastore, M. Tonks, P. Millett, B. Dorado, D. R. Gaston, D. Andrs, R. L. Williamson, R. C. Martineau, B. P. Uberuaga, and C. R. Stanek. Atomistic modeling of intrinsic and radiation-enhanced fission gas (Xe) diffusion in $UO_{2\pm x}$: Implications for nuclear fuel performance modeling. *Journal of Nuclear Materials*, 451:225–242, 2014.

[33] D. A. Andersson, M. R. Tonks, L. Casillas, S. Vyas, P. Nerikar, B. P. Uberuaga, and C. R. Stanek. Multiscale simulation of xenon diffusion and grain boundary segregation in UO_2. *Journal of Nuclear Materials*, 462:15–25, 2015.

[34] E. Vathonne, D. A. Andersson, M. Freyss, R. Perriot, M. W. D. Cooper, C. R. Stanek, and M. Bertolus. Determination of Krypton Diffusion Coefficients in Uranium Dioxide Using Atomic Scale Calculations. *Inorganic Chemistry*, 56:125–137, 2017.

[35] D. A. Andersson, B. P. Uberuaga, P. V. Nerikar, C. Unal, and C. R. Stanek. U and Xe transport in $UO_{2\pm x}$: Density functional theory calculations. *Physical Review B - Condensed Matter and Materials Physics*, 84:1–12, 2011.

[36] C. R. A. Catlow. Theory of fission gas migration in UO_2. *Radiation Effects*, 53:127–132, 1980.

[37] R. Perriot, C. Matthews, M. W. D. Cooper, B. P. Uberuaga, C. R. Stanek, and D. A. Andersson. Atomistic modeling of out-of-pile xenon diffusion by vacancy clusters in UO_2. *Journal of Nuclear Materials*, 520:96–109, 2019.

[38] C. Matthews, R. Perriot, M. W. D. Cooper, C. R. Stanek, and D. A. Andersson. Cluster dynamics simulation of uranium self-diffusion during irradiation in UO_2. *Journal of Nuclear Materials*, 527:151787, 2019.

[39] C. Matthews, R. Perriot, M. W. D. Cooper, C. R. Stanek, and D. A. Andersson. Cluster Dynamics Simulation of Xenon Diffusion During Irradiation in UO_2. *Journal of Nuclear Materials*, 540:152326, 2020.

[40] T. Watanabe, S. B. Sinnott, J. S. Tulenko, R. W. Grimes, P. K. Schelling, and S. R. Phillpot. Thermal transport properties of uranium dioxide by molecular dynamics simulations. *Journal of Nuclear Materials*, 375:388–396, 2008.

[41] D. D. Lanning, C. E. Beyer, and K. J. Geelhood. FRAPCON-3 Updates, Including Mixed-Oxide Fuel Properties. NUREG/CR-6534, Vol. 4 PNNL-11513. Technical report. Pacific Northwest National Laboratory, Richmond, USA, 2005.

[42] A. Marion. (NEI) letter dated June 13, 2006 to H. N. Berkow (USNRC/NRR). Safety Evaluation by the Office of Nuclear Reactor Regulation of Electric PowerResearch Institute (EPRI) Topical Report TR-1002865, "Topical Report on Reactivity Initiated Accidents: Bases for RIA Fuel rod Failures and Core Coolability Criteria". http://pbadupws.nrc.gov/docs/ML0616/ML061650107.pdf.

[43] M. R. Tonks, X. Y. Liu, D. A. Andersson, D. Perez, A. Chernatynskiy, G. Pastore, C. R. Stanek, and R. Williamson. Development of a multiscale thermal conductivity model for fission gas in UO_2. *Journal of Nuclear Materials*, 469:89–98, 2016.

[44] J. K. Fink. Thermophysical properties of uranium dioxide. *Journal of Nuclear Materials*, 279:1–18, 2000.

[45] S. Kashibe, K. Une, and K. Nogita. Formation and growth of intragranular fission gas bubbles in UO_2 fuels with burnup of 6–83 GWd/t. *Journal of Nuclear Materials*, 206:22–34, 1993.

[46] C. M. Allison, G. A. Berna, R. Chambers, E. W. Coryell, K. L. Davis, D. L. Hagrman, D. T. Hagrman, N. L. Hampton, J. K. Hohorst, R. E. Mason, M. L. McComas, K. A. McNeil, R. L. Miller, C. S. Olsen, G. A. Reymann, and L. J. Siefken. SCDAP/RELAP5/MOD3.1 code manual, volume IV: MATPRO–A library of materials properties for light-water-reactor accident analysis. NUREG/CR-6150, EGG-2720. Technical report. Idaho National Laboratory, Idaho Falls, USA, 1993.

[47] J. B. Ainscough, B. W. Oldfield, and J. O. Ware. Isothermal grain growth kinetics in sintered UO_2 pellets. *Journal of Nuclear Materials*, 49:117–128, 1973.

[48] F. S. Ham. Theory of diffusion-limited precipitation. *Journal of Physics and Chemistry of Solids*, 6:335–351, 1958.

[49] R. J. White and M. O. Tucker. A new fission-gas release model. *Journal of Nuclear Materials*, 118:1–38, 1983.

[50] D. Pizzocri, G. Pastore, T. Barani, A. Magni, L. Luzzi, P. Van Uffelen, S. A. Pitts, A. Alfonsi, and J. D. Hales. A model describing intra-granular fission gas behaviour in oxide fuel for advanced engineering tools. *Journal of Nuclear Materials*, 502:323–330, 2018.

[51] B. Therache. The High Initial Rating Test, IFA-677.1: Results after First Cycle of Irradiation. Technical Report HWR-819, Organisation for Economic Co-operation and Development Halden Reactor Project, Halden, Norway, 2005.

[52] T. Tverberg. Update on the in-pile results from the fission gas release mechanisms study in IFA-716. Technical Report HWR-1090, Organisation for Economic Co-operation and Development Halden Reactor Project, Halden, Norway, 2014.

[53] Y. Rashid, R. Dunham, and R. Montgomery. Fuel analysis and licensing code: FALCON MOD01, EPRI 1011308. Technical report, 2004.

[54] T. Barani, D. Pizzocri, G. Pastore, L. Luzzi, and J. D. Hales. Isotropic softening model for fuel cracking in BISON. *Nuclear Engineering and Design*, 342:257–263, 2019.

[55] Ch. Riglet-martial, Ph. Martin, D. Testemale, C. Sabathier-Devals, G. Carlot, and P. Matheron. X. Iltis, U. Pasquet, C. Valot, C. Delafoy, and R. Largenton. Thermodynamics of chromium in UO_2 fuel: A solubility model. *Journal of Nuclear Materials*, 447:63–72, 2014.

[56] M. W. D. Cooper, C. R. Stanek, and D. A. Andersson. The role of dopant charge state on defect chemistry and grain growth of doped UO_2. *Acta Materialia*, 150:403–413, 2018.

[57] S. C. Middleburgh, D. C. Parfitt, R. W. Grimes, B. Dorado, M. Bertolus, P. R. Blair, and L. Hallstadius. Solution of trivalent cations into uranium dioxide. *Journal of Nuclear Materials*, 420:258–261, 2012.

[58] H. Lukas, S. G. Fries, B. Sundman. Computational Thermodynamics: The Calphad Method. *1st edition*, *Cambridge University Press*, *New York*, *NY, USA*, 2007.

[59] J. O. Andersson, T. Helander, L. Höglund, P. F. Shi, and B. Sundman. Thermo-Calc and DICTRA, Computational tools for materials science. *Calphad*, 26:273–312, 2002.

[60] C. Guéneau, N. Dupin, B. Sundman, C. Martial, J.-C. Dumas, S. Gossé, S. Chatain, F. De Bruycker, D. Manara, and R. J. M. Konings. Thermodynamic modelling of advanced oxide and carbide nuclear fuels: Description of the U–Pu–O–C systems. *Journal of Nuclear Materials*, 419:145–167, 2011.

[61] Thermo-Calc Software SGTE Substances database version 6 (accessed 16 June 2019).

[62] T. B. Lindemer and T. M. Besmann. Chemical Thermodynamic Representation of UO_{2+x}. *Journal of Nuclear Materials*, 130:473–488, 1985.

[63] M. W. Chase. NIST-JANAF Thermochemical Tables. *Journal of Physical and Chemical Reference Data Monographs*, 9:1, 1998.

[64] F. A. Kroger and H. J. Vink. *Journal of Solid State Physics*, 3:307–435, 1956.

[65] J. Schoenes. Electronic transitions, crystal field effects and phonons in UO_2. *Physics Reports*, 63:301–336, 1980.

[66] A. C. S. Sabioni, W. B. Farraz, and F. Millot. First study of uranium self-diffusion in UO_2 by SIMS. *Journal of Nuclear Materials*, 257:180–184, 1998.

[67] C. Baker. The fission gas bubble distribution in uranium dioxide from high temperature irradiated SGHWR fuel pin. *Journal of Nuclear Materials*, 66:283–291, 1977.

[68] O. Brémont. IFA-716.1 Fission gas release mechanisms. Technical Report HWR-1008, Organisation for Economic Co-operation and Development Halden Reactor Project, Halden, Norway. 2008.

[69] J. Julien, C. Bassi, A Bouloré, C. Struzik, B. Baurens, and C. Delafoy. Analysis of IFA-716-6 tests results using the ALCYONE fuel code. *Proc. of the Enlarged Halden Programme Group Meeting*, *Sandefjord*, *Norway*, May 19-24, 2019.

[70] J. Klouzal. Proposal for the testcase for the data validation and treatment. Presented at the HRP Workshop on F&M Legacy Database, Organisation for Economic Co-operation and Development, Boulogne-Billancourt, France, November 19, 2018.

[71] W. Wiesenack. Verification and improvement of test data for the HRP Legacy Data Base. *Proc. of the Enlarged Halden Programme Group Meeting*, Sandefjord, Norway, May 19-24, 2019.

M. W. D. Cooper: Conceptualization, Methodology, Investigation, Visualization, Writing - Original Draft. **G. Pastore:** Conceptualization, Software, Methodology, Visualization, Investigation, Writing - Original Draft. **Y. Che:** Methodology, Investigation, Writing - Original Draft. **C. Matthews:** Methodology, Software, Writing - Review & Editing. **A. Forslund:** Investigation, Visualization, Writing - Review & Editing. **C. R. Stanek:** Conceptualization, Supervision, Writing - Review & Editing. **K. Shirvan:** Supervision, Writing - Review & Editing. **T. Tverberg:** Data Curation, Writing - Review & Editing. **KA Gamble:** Writing - Review & Editing. **B. Mays:** Writing - Review & Editing. **D. A. Andersson:** Conceptualization, Supervision, Methodology, Writing - Review & Editing.

Declaration of interests

☒ The authors declare that they have no known competing financial interests or personal relationships that could have appeared to influence the work reported in this paper.

☐The authors declare the following financial interests/personal relationships which may be considered as potential competing interests: